# Adaptive refinement and selection process through defect localization for reconstructing an inhomogeneous refraction index

Yann Grisel, Vincent Mouysset, Pierre-Alain Mazet, Jean-Pierre Raymond

# Adaptive refinement and selection process through defect localization for reconstructing an inhomogeneous refraction index

Y. Grisel[1], V. Mouysset[2], P. A. Mazet[2] and J. P. Raymond[3]

[1] *UPPA - IUT de Mont-de-Marsan, 40004 Mont-de-Marsan, France*

[2] *Onera - The French Aerospace Lab, 31055 Toulouse, France*

[3] *Université Paul Sabatier, Institut de Mathématiques de Toulouse, 31062 Toulouse, France*

**Abstract.** We consider the iterative reconstruction of both the internal geometry and the values of an inhomogeneous acoustic refraction index through a piecewise constant approximation. In this context, we propose two enhancements intended to reduce the number of parameters to reconstruct, while preserving accuracy. This is achieved through the use of geometrical informations obtained from a previously developed defect localization method. The first enhancement consists in a preliminary selection of relevant parameters, while the second one is an adaptive refinement to enhance precision with a low number of parameters. Each of them is numerically illustrated.

## 1 Introduction

We are interested in the inverse medium problem consisting in the reconstruction of an inhomogeneous acoustic refraction index from far-field measurements generated through plane waves. This parameter identification problem is non-linear and ill-posed, and we investigate two methods to reduce the number of computed parameters while preserving the reconstruction accuracy. Applications are, for example, non-destructive structure testing or biomedical imaging [1, 2, 3].

Following the abundant literature, we write the inverse medium problem as a least-squares problem (see [4] and references therein). Besides, since we consider discontinuous indices, we look for the index of refraction as a piecewise constant function. In this setting, for its ease of implementation and its efficiency for reasonably sized problems, we consider the Gauss-Newton method, applied to a cost functional involving a Tikhonov regularization [5]. However, the Gauss-Newton method treats all parameters in the same way. Yet, during the reconstruction, or even right from the beginning, the values of some parameters can be close to the exact value, while other parameters will need more iterations before reaching a given accuracy. In the absence of some local information, the accurate parameters are then uselessly updated at each iteration. Thus, we explore two uses of geometrical informations, obtained through defect localization, to focus the reconstruction and consequently lighten its numerical cost.

By defect localization, we mean localizing the support of a perturbation with respect to some known reference. However, in this paper, it is the reconstructed index that we use as the known reference, and it is the exact index that we use as an unknown perturbed state. Thus, defect localization can be used to locate errors in the index reconstruction. Besides, it has recently been proved that the location of the defects in a given refraction index could be established from far-field measurements of the unknown state and computed through a fast numerical method [6, 7]. Also, shape reconstruction has already been used jointly with parameter identification by using the *Linear Sampling* method [8, 9, 10, 11].

However, the *Factorization method* approach, involved in [6] and [7], provides a more straightforward formulation as an equivalence that is defined at each point. So, we propose here to use

this fast local information to reduce the computational effort in the complete refraction index reconstruction process.

More precisely, in this paper we are going to propose two hybridizations between Gauss-Newton and defect localization methods. We first consider the case where a known index has been locally modified. This could happen, for instance, from a local deterioration or a partially incorrect estimation of the actual index. In this case, a preliminary defect localization provides a geometrical information that we can use to choose which parameters have to be reconstructed. Then, the reconstruction can be performed straightforwardly on a reduced computational domain. The goal of this strategy is to avoid the useless reconstruction of parameters for which we have a suitable initial guess. In a second time, we investigate adaptive refinement. Here, defect localization is used to exhibit inaccurate regions in the current reconstruction. This local information allows us to refine the reconstruction mesh in these regions and resume the reconstruction to get a better precision while restraining the number of computed parameters. With this strategy, we thus aim to control the numerical effort by diminishing the number of discrete parameter values with respect to an uniform mesh of the whole parameter space.

This paper is structured as follows: In section 2, we specify the mathematical setting. We then introduce the direct problem in section 2.1, followed in section 2.2 by the description of the inverse medium problem we are interested in. The numerical method on which we will build our enhancements is then described in section 2.3. Afterwards, the defect localization and its applications are presented in section 3. We show how to reduce the reconstruction domain in section 3.1, and the adaptive refinement process is detailed in section 3.2. Finally, we numerically illustrate the sequence of both applications, and furthermore on a non-trivial example, in section 4. We end the the paper by concluding remarks in section 5.

# 2 Presentation of the problem

We start by introducing the direct problem and the inverse medium problem, followed by its numerical treatment.

## 2.1 The direct problem

We consider time-harmonic acoustic waves, with a fixed wave number $k$, modeled by the Helmholtz equation [12]. Inhomogeneous media are then represented by an acoustic refraction index, denoted by $n \in L^\infty(\mathbb{R}^d)$. So, the total field, denoted by $u_n \in L^2_{loc}(\mathbb{R}^d)$, is assumed to satisfy

$$\Delta u_n + k^2 n(x) u_n = 0, \quad x \in \mathbb{R}^d, \tag{1}$$

where $d$ is the problem's dimension ($d = 2$ or $3$). We consider compactly supported inhomogeneities, and we denote by $D$ the support of $n(x) - 1$. We also denote by $u^i \in L^2_{loc}(\mathbb{R}^d)$ an incoming wave satisfying (1) with $n(x) = 1$ . The total field is then the sum of this incoming wave and the wave scattered by the inhomogeneous medium, denoted by $u^s \in L^2_{loc}(\mathbb{R}^d)$:

$$u_n := u^s + u^i, \tag{2}$$

where the scattered wave is assumed to satisfy the Sommerfeld radiation condition

$$\partial_r u^s = iku^s + o\Big(|x|^{-\frac{d-1}{2}}\Big). \tag{3}$$

Then, the linear system (1)-(3) defines $u_n \in L^2_{loc}(\mathbb{R}^d)$ uniquely from $u^i$ [12, Chap. 8].

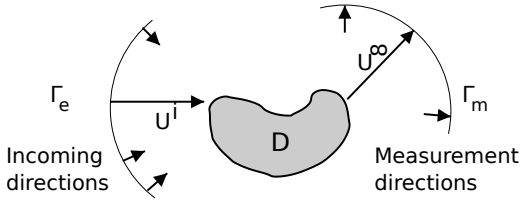


Figure 1: General setting and notations.

Besides, the outgoing part of a wave has an asymptotic behavior called the far field pattern, denoted by $u_n^\infty \in \mathcal{C}^\infty(\Gamma_m)$, and given by the Atkinson expansion [13, Theorem 6.11]

$$u_n(x) := u^i(x) + \gamma \frac{e^{ik|x|}}{|x|^{\frac{d-1}{2}}} u_n^\infty(\vec{x}) + o\Big(|x|^{-\frac{d-1}{2}}\Big), \quad \vec{x} := \frac{x}{|x|} \in \Gamma_m, \tag{4}$$

where $\Gamma_m$ denotes the set of measurement directions as a subset of the unit sphere $S^{d-1}$ (see figure 1), and where $\gamma$ only depends on the dimension and is defined by

$$\gamma := \begin{cases} \frac{e^{i\pi/4}}{\sqrt{8\pi k}} & \text{if d=2,} \\ \frac{1}{4\pi} & \text{if d=3.} \end{cases}$$

Furthermore, for practical reasons, we will mainly consider scattered waves having a plane wave source. These plane waves are defined by

$$u^i(\vec{\theta}, x) := \exp(ik\vec{\theta} \cdot x),$$

where $\vec{\theta}$ is a unitary vector in the set of incidence directions, denoted by $\Gamma_e$ as shown in Figure 1. We then denote the total field with a plane wave source of incoming direction $\vec{\theta}$ by

$$u_n(\vec{\theta}, x), \quad \vec{\theta} \in \Gamma_e,\ x \in \mathbb{R}^d.$$

Lastly, the corresponding far-field pattern in the measurement direction $\vec{x} \in \Gamma_m$ will be denoted by

$$u_n^\infty(\vec{\theta}, \vec{x}), \quad \vec{\theta} \in \Gamma_e,\ \vec{x} \in \Gamma_m.$$

## 2.2 The inverse medium problem

We are interested in the reconstruction, from far-field data, of an inhomogeneous refraction index that will be denoted by $n^\star \in L^\infty(D)$ throughout this paper. Note that all considered indices will be implicitly extended by 1 outside $D$, the compact support of $n^\star - 1$.

Most of the methods used to solve this reconstruction problem are valid for domains that are (subsets of) Hilbert spaces. Thus, we consider an index-to-far-field mapping $\mathcal{F} : L^\infty(D) \to L^2(\Gamma_e \times \Gamma_m)$ defined by

$$\mathcal{F}(n) := u_n^\infty.$$

Besides, data are generally perturbed by noise or measurement errors. So, we assume that we only have access to $\mathfrak{u}^\varepsilon \in L^2(\Gamma_e \times \Gamma_m)$, the perturbed version of $u_{n^\star}^\infty$ satisfying

$$\|\mathfrak{u}^\varepsilon - u_{n^\star}^\infty\|_{L^2(\Gamma_e \times \Gamma_m)} \leqslant \varepsilon \|u_{n^\star}^\infty\|_{L^2(\Gamma_e \times \Gamma_m)}. \tag{5}$$

The usual approach to this problem is then to find $n$ by minimizing the difference between $\mathcal{F}(n)$ and $\mathfrak{u}^\varepsilon$. Thus, we define the data misfit by

$$J(n) := c_1 \left\| \mathcal{F}(n) - \mathfrak{u}^\varepsilon \right\|^2_{L^2(\Gamma_e \times \Gamma_m)},$$

where $c_1$ denotes a normalization constant (*e.g.* $c_1 = \|\mathfrak{u}^\varepsilon\|^{-2}_{L^2(\Gamma_e \times \Gamma_m)}$).

Even so, this problem is not continuous, as is shown by the following proposition. So, even a small perturbation $\varepsilon$ can lead to a minimizer very far from $n^\star$.

**Proposition 2.1.** *The non-linear problem consisting in "finding $n_\varepsilon$ minimizing $J$" is ill-posed in the sense of Hadamard.*

*Proof.* The mapping $\mathcal{F}$ is compact, and thus cannot have a continuous inverse.

Indeed, it has been shown in [14, Proposition 2.1.14] that the mapping $n \mapsto u_n$ is continuous from $L^\infty(D)$ into $H^2(D)$; and as such, from $L^\infty(D)$ into $L^2(D)$. As a consequence, the same property holds for the mapping $f : n \mapsto (n-1)u_n$.

Moreover, the asymptotic behavior of the Lippmann-Schwinger equation yields the following relationship [12, Chap. 8.4]:

$$\mathcal{F}(n)(\vec{\theta}, \vec{x}) = \int_{z \in D} e^{-ik\vec{x}\cdot z} k^2 (n(z) - 1) u_n(\vec{\theta}, z), \quad \theta \in \Gamma_e,\ \vec{x} \in \Gamma_m. \tag{6}$$

It is well known that the linear operator $f \mapsto \int_{z \in D} e^{-ik\vec{x}\cdot z} k^2 f(z)$ is compact.

Hence, the non-linear operator $\mathcal{F}$ is the combination of a compact linear operator with a continuous mapping. Therefore, it is compact itself. □

## 2.3 Iterative approximation by a piecewise constant index

As stated in the introduction, we try to recover the unknown index $n^\star$ with help of piecewise constant functions. Hence, the indices will numerically be represented by $N$ complex parameters $(\eta_i)_{i=1\ldots N}$ associated to the same number of zones $(Z_i)_{i=1\ldots N}$, so $n(x) = \sum_{i=1\ldots N} \eta_i \mathbf{1}_{Z_i}(x)$, where $\mathbf{1}_{Z_i}(x)$ is the characteristic function of $Z_i$ and $\bigcup_{i=1\ldots N} Z_i = D$. Each zone is thus a set of connected elements in the underlying mesh used to solve the Helmholtz equation. Moreover, to avoid any possibility of inverse crime, the reconstruction will be led on a second mesh that is different from the one used to generate the data $\mathfrak{u}^\varepsilon$. As a consequence, the zones associated to the unknown parameters will intersect the discontinuities of $n^\star$. It is thus strictly impossible to reconstruct $n^\star$ exactly. This is illustrated in Figure 2, showing two 2D meshes that will be used in our numerical simulations.

In this setting, we use the well-known Gauss-Newton method applied to the cost function $J$ with a standard Tikhonov regularization term [15]:

$$\widetilde{J}(n) := c_1 \left\| \mathcal{F}(n) - \mathfrak{u}^\varepsilon \right\|^2_{L^2(\Gamma_e \times \Gamma_m)} + c_2 \left\| n - n_0 \right\|^2_{L^2(D)},$$

where $c_2 > 0$ is a regularization parameter and $n_0 \in L^\infty(D)$ is an initial guess. The choice of this regularization parameter parameter is discussed in a large number of papers, see for example [16, 17] and references therein. Empirically, it seems that a few percent of the fidelity term $c_1 \left\| \mathcal{F}(n) - \mathfrak{u}^\varepsilon \right\|^2$ are a decent initial guess for $c_2$. Besides, assumptions on $n_0$ and $c_2$ for the convergence of this method are discussed in [18, 19]. Hence, the index $n^\star$ we are looking for is approximated by a sequence $(n_p)_{p \in \mathbb{N}}$ of indices, defined iteratively through Algorithm 1.

The gradient of the cost function, required for the Gauss-Newton method, has the following integral representation.

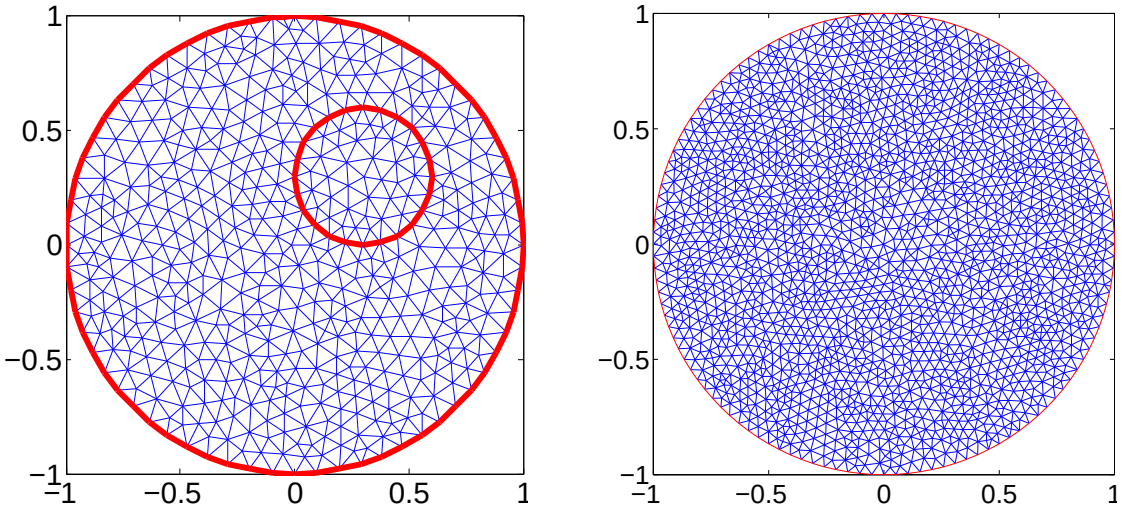


(a) Data mesh

(b) Reconstruction mesh

Figure 2: Test case geometry

**Algorithm 1:** The Gauss-Newton method for $\widetilde{J}$

**Input**: $n_0 \in L^\infty(D)$

$p \leftarrow 0$;

**repeat**

Compute $n_{p+1}$ by solving the linear system

$$\big(D\mathcal{F}(n_p)^\star D\mathcal{F}(n_p) + \frac{c_2}{c_1} id\big)(n_{p+1} - n_0) =$$
$$-D\mathcal{F}(n_p)^\star \big(\mathcal{F}(n_p) - \mathfrak{u}^\varepsilon - D\mathcal{F}(n_p)(n_p - n_0)\big),$$

where $id$ is the identity matrix, and $D\mathcal{F}(n_p)^\star$ is the hermitian adjoint of the matrix $D\mathcal{F}(n_p)$;

$p \leftarrow p + 1$;

**until** $\|n_p - n_{p-1}\|_2 / (1 + \|n_{p-1}\|_2) < \epsilon$;

**Output**: $n_{p_{\text{End}}}$

**Lemma 2.2.** *The mapping $\mathcal{F}$ is differentiable and the differential $D\mathcal{F}$ evaluated at $n \in L^\infty(D)$ and applied to the direction $dn \in L^\infty(D)$ has the following integral representation*

$$D\mathcal{F}(n)\,dn : (\vec{\theta}, \vec{x}) \mapsto \int_{z\in D} k^2 u_n(-\vec{x}, z) u_n(\vec{\theta}, z)\, dn(z)\, dz, \quad \vec{\theta} \in \Gamma_e,\ \vec{x} \in \Gamma_m. \tag{7}$$

*Proof.* Expansion (4) shows that $u_n^\infty(\vec{\theta}, \cdot)$ is linear with respect to the scattered field $(u_n - u^i)(\vec{\theta}, \cdot)$. Furthermore, It has been shown in [14, Proposition 4.3.1] that the scattered field is differentiable with respect to $n$ and that the differential of the index-to-scattered-field mapping evaluated at $n \in L^\infty(D)$, applied to $dn \in L^\infty(D)$, is the function $v^s(\vec{\theta}, \cdot) \in L^2_{loc}(\mathbb{R}^d)$ satisfying

$$\left(\Delta_x + k^2 n(x)\right) v^s(\vec{\theta}, x) = -k^2\, u_n(\vec{\theta}, x)\, dn(x), \quad x \in \mathbb{R}^d, \tag{8}$$

and the Sommerfeld radiation condition (3). Note that, contrarily to $n$, the direction $dn$ is extended by 0 outside $D$. Thus, $\mathcal{F}$ is differentiable, and its differential is defined on $\mathcal{C}^\infty(\Gamma_e \times \Gamma_m)$ by $D\mathcal{F}(n)\,dn = v^\infty$.

Now, let us denote by $\Phi_n(z, x)$ the Green function of the Helmholtz equation (1). Multiplying (8) by $\Phi_n(z, x)$, integrating over $D$, and using Green's formula, yields

$$v^s(\vec{\theta}, x) = \int_{z\in D} k^2 \Phi_n(z, x) u_n(\vec{\theta}, z)\, dn(z)\, dz, \quad x \in \mathbb{R}^d.$$

The asymptotic behaviour is then given by

$$v^\infty(\vec{\theta}, \vec{x}) = \int_{z\in D} k^2 \Phi_n^\infty(z, \vec{x}) u_n(\vec{\theta}, z)\, dn(z)\, dz, \quad \vec{x} \in S^{d-1}.$$

Finally, representation (7) is obtained by applying the mixed reciprocity principle: $\Phi_n^\infty(z, \vec{x}) = u_n(-\vec{x}, z)$ (see [20, equation (3.66)]). □

**Remark 2.3.** *As described in [18, 19], to ensure the convergence of the regularized non-linear Gauss-Newton method (Algorithm 1), one also requires the differential of $\mathcal{F}$ to be Lipschitz continuous, which is actually the case. Indeed, the reference [14, Proposition 4.3.1], invoked in the proof of Lemma 2.2, gives the twice continuous differentiability of the scattered field with respect to $n$, thus implying that $\mathcal{F}$ is twice continuously differentiable too.*

### Numerical example

**Set-up** To illustrate our reconstruction schemes in $\mathbb{R}^2$, we consider a disc $D$ of radius 1 centered at the origin. The embedded perturbation $\Omega$ is then chosen as another disc centered at $(0.3, 0.3)$, and of radius 0.3. The mesh corresponding to this geometry can be seen in Figure 2a. The (perturbed) index we are looking for is set to $n^\star := 1.3$ in $D \setminus \Omega$ and $n^\star := 1.6$ in $\Omega$ whereas the initial guess, corresponding to the last known state, is $n_0 := 1.3$ in $D$.

The Gaus-Newton method is performed with the regularization parameter $c_2 := 10^{-2}$ (and $c_1 = \|\mathfrak{u}^\varepsilon\|^{-2}_{L^2(\Gamma_e\times\Gamma_m)}$, as previously denoted). Also, solutions to the Helmholtz equation are computed *via* a $P^1$ finite element method and Cartesian Perfectly Matched Layers (PML) [21]. Lastly, the corresponding far-fields are evaluated through the representation formula (6). For all these examples, the wave number is set to $k = 5$, and the angles corresponding to incoming/measurement directions are equally distributed over $[0, 2\pi]$.

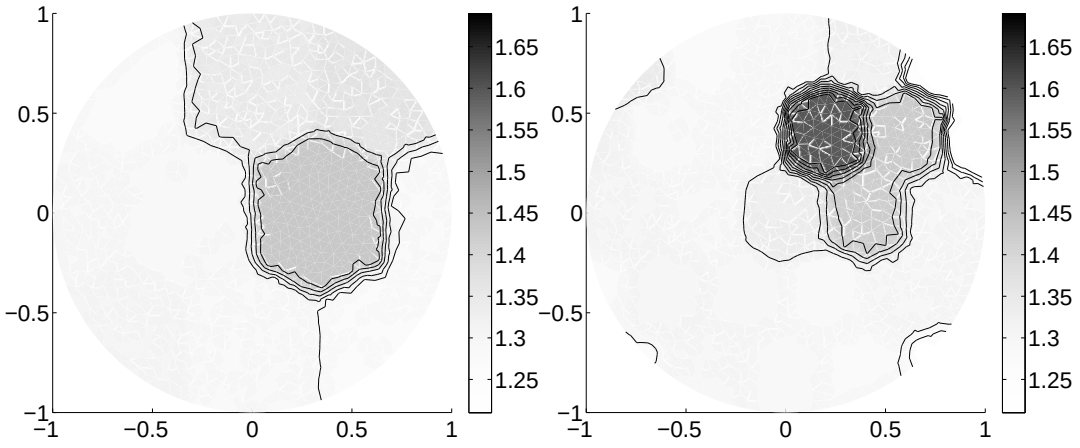


(a) $N = 10$ parameters

(b) $N = 27$ parameters

(c) $N = 75$ parameters

(d) $N = 2672$ parameters

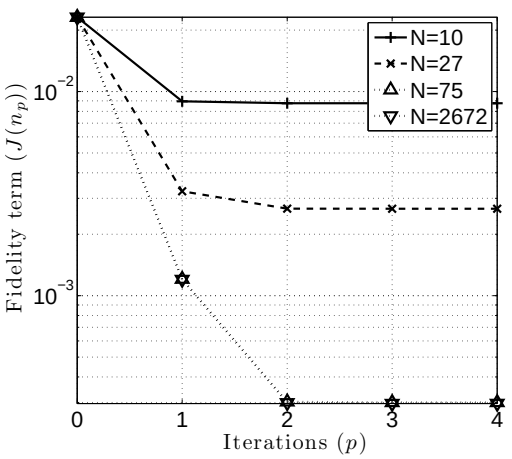


(e) Evolution of the fidelity term

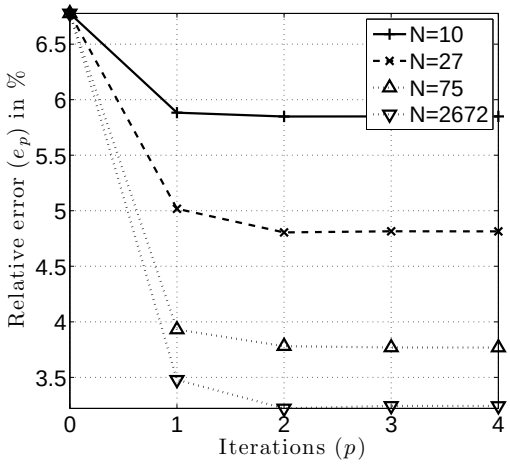


(f) Evolution of the relative error

Figure 3: Gauss-Newton reconstruction with $30 \times 30$ data and $\varepsilon = 2\%$ noise

**Results** An example can be seen in Figure 3 with a reconstruction mesh of 2672 triangles (see Figure 2b) divided into $N = 10$, $N = 27$, $N = 75$ and $N = 2672$ zones.

More precisely, the final relative error

$$e_{p_{\text{End}}} := \|n_{p_{\text{End}}} - n^\star\|_{L^2(D)} \,/\, \|n^\star\|_{L^2(D)}$$

is synthesized as a function of the number of zones $N$ in Figure 4.

Moreover, for comparison purpose, we list in Table 1 the exact final relative error obtained in several configurations. Besides, we see in this table that the relative error is of order $10^{-2}$, so we choose the stopping criterion $\|n_p - n_{p-1}\|_2 \,/(1+\|n_{p-1}\|_2) < \epsilon = 10^{-4}$ for all our reconstructions. In all these test cases, this bound was reached after four iterations.

**Comments** The low error that can be seen in Figure 4 for $N = 19$ is a particular case related to the considered test case. Indeed, it just happens that this choice of zones provides a natural match to our simple geometry, yielding a reconstruction that is better than expected.

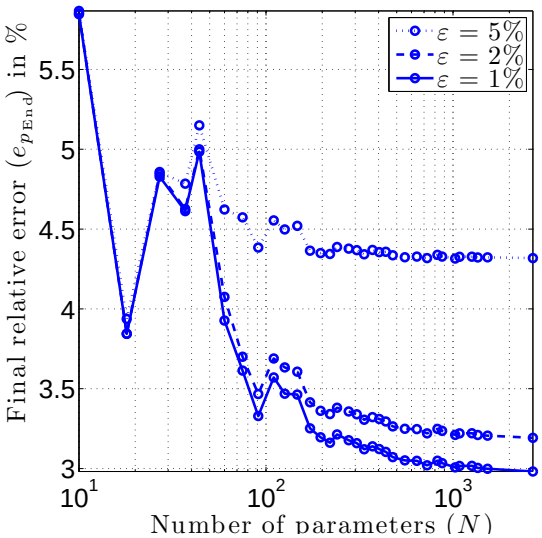


Figure 4: Final relative error with $30 \times 30$ data and different noise levels $\varepsilon$

# 3 Enhancements of the Gauss-Newton method via defect localization

In the presented piecewise constant iterative approximation, the possible precision is directly linked to the number of basis functions $N$ which, in turn, is linked to the computational effort. In the lack of some geometrical informations, all parameters are equally treated and updated at each iteration. However, this can generate more effort than is really needed, and we address two cases where these unnecessary efforts can be reduced.

1. For the first case, we consider a bounded perturbation in a known initial state $n_0$. So, most of the values of the index have not changed and should not be reconstructed.

| $N$ | $\varepsilon$ | $15 \times 15$ data $e_{p_{\text{End}}}$ | $30 \times 30$ data $e_{p_{\text{End}}}$ | $60 \times 60$ data $e_{p_{\text{End}}}$ |
|---|---|---|---|---|
| 10 | 5% | 5.9% | 5.9% | 5.9% |
| | 2% | 5.9% | 5.9% | 5.8% |
| | 1% | 5.9% | 5.8% | 5.8% |
| 27 | 5% | 4.9% | 4.9% | 4.9% |
| | 2% | 4.8% | 4.8% | 4.8% |
| | 1% | 4.9% | 4.8% | 4.8% |
| 75 | 5% | 5.4% | 5.0% | 4.4% |
| | 2% | 3.9% | 3.7% | 3.7% |
| | 1% | 3.6% | 3.6% | 3.6% |
| 2672 | 5% | 5.3% | 4.5% | 3.9% |
| | 2% | 3.5% | 3.3% | 3.1% |
| | 1% | 3.1% | 3.0% | 2.9% |

Table 1: Gauss Newton reconstruction

2. For the second case, we are concerned in focusing on the most inexact constants during the reconstruction. Indeed, to obtain a precise identification, the reconstruction mesh has to be refined in the zones intersected by the discontinuities of $n^\star$. However, if $n^\star$ is constant in large areas, refining the reconstruction mesh everywhere only raises the computational effort for a relatively small precision increment.

To address these aspects of the reconstruction, the useful information in both cases would thus be the localization of the nearly exact constants. Or, to put it otherwise, we look for the localization of the difference between the reconstruction at hand and the exact (unknown) index. We call this defect localization with respect to an inhomogeneous background reference. Of course, to enhance the complete reconstruction, access to this specific information should be fast. To this end, it has been shown in [6] that the Factorization method for a constant background, as presented in [22], can be extended to an inhomogeneous background with help of a modified measurement operator.

**Theorem 3.1.** *[6, Theorem 6.1] Assume that $\Gamma_m = \Gamma_e = S^{d-1}$. Then, define a measurement operator $W := \left(Id + 2ik\,|\gamma|^2\, F_n\right)(F_{n^\star} - F_n)$, where $F_n : L^2(S^{d-1}) \to L^2(S^{d-1})$ denotes the classical far-field operator, defined by $F_n g(\vec{x}) := \langle g, \overline{u_n^\infty(\cdot, \vec{x})}\rangle_{L^2(S^{d-1})}$. Next, we define the positive self-adjoint operator $W_\#$ by $W_\# := |W + W^\star| + |W - W^\star|$, where the notation $|\cdot|$ applied to an operator $L$ stands for $|L| := (L^\star L)^{\frac{1}{2}}$. Lastly, assume that $n$ and $n^\star$ are real valued, and that either $(n - n^\star)$ or $(n^\star - n)$ is locally bounded from below in $\Omega := \text{support}(n - n^\star)$.*

*Then, for each $z \in \mathbb{R}^d$, we have $n(z) \neq n^\star(z)$ if, and only if,*

$$\mathcal{S}_{\{n,n^\star\}}(z) := \left( \sum_j \frac{\left| \langle \overline{u_n(\cdot, z)}, \psi_j \rangle_{L^2(S^{d-1})} \right|^2}{\sigma_j} \right)^{-1} > 0,$$

*where $(\sigma_j, \psi_j)$ is an eigensystem of $W_\#$.*

**Remark 3.2.** *This localization result calls for a number of remarks.*

1. *Theorem 3.1 requires full bi-static data ($\Gamma_m = \Gamma_e = S^{d-1}$) and real-valued indices. However, we also recall the conjecture, stated in [6, Remark 6.2]: To build the localization function $\mathcal{S}$, the eigensystem of $W_\#$, denoted by $(\sigma_j, \psi_j)$, could be replaced by a right-singular system of $(F_{n^\star} - F_n)$. The main benefit is the possibility of considering $\Gamma_m \neq \Gamma_e \neq S^{d-1}$ and complex valued indices. Moreover, we* a priori *need to truncate the sum to avoid over-valued terms, due to perturbations on the smallest eigenvalues. However, in our experience, we have noticed that the computations are stable. So, no truncation is performed for the numerical applications of this paper and all the eigenvalues of the measurement operator's matrix representation are considered.*

2. *Furthermore, numerical examples in [6] show that this localization is effective for defects bigger than (approximately) one over six of the wavelength. Besides, in order to get satisfactory results in the successive resolutions of the Helmholtz equation, we have set the reconstruction mesh size to be about one over twenty of the wavelength. Thus, we will only consider defects that cover at least four connected mesh elements.*

3. *Moreover, the examples shown in [6] exhibit that defects can be localized even when the surrounding background is not precisely known. Practically, low amplitude inaccuracies with respect to the exact index do not seem to interfere with the localization of the contrasting defects. Thus, geometrical information gained through the defect localization presented here is expected to focus on the most "defective" zones.*

4. *Finally, it is to be noted that the added computational cost of this localization function within the Gauss-Newton process will be negligible. Indeed, the functions $u_n(\cdot, z)$ will already have been computed to evaluate the differential of $\mathcal{F}$, as can be seen on the integral representation (7).*

## 3.1 Selective reconstruction

We here consider the case where the initial guess $n_0$ is exact, except for some perturbation whose support will be denoted by $\Omega$. Thus, we propose to perform a preliminary selection of the parameters, to reconstruct only the perturbed ones. The selection is performed by considering only the parameters associated to zones where the maximal value of the (normalized) defect localization function $\mathcal{S}_{\{n_0,n^\star\}} / \max_D \mathcal{S}_{\{n_0,n^\star\}}$ is above some threshold $\mathcal{T}$. The whole index $n^\star$ is then reconstructed by updating those parameters only. This leads to a reconstruction, described in Algorithm 2, using a number of parameters $N_{Sel}$ that should be significantly less than $N$.

**Algorithm 2:** Selective reconstruction

**Input**: $n_0 \in L^2(D)$

$\mathcal{S}_i \leftarrow \max_{Z_i} \mathcal{S}_{\{n_0,n^\star\}}(x)$;

$\Omega_\mathcal{T} \leftarrow$ the set of zones for which $\mathcal{S}_i > \mathcal{T} \max \mathcal{S}_i$;

$n_{p_{\text{End}}} \leftarrow$ **Algorithm 1**$(\mathbf{n_0}_{|\mathbf{\Omega}_\mathcal{T}})$ (all indices are extended by $n_0$ outside $\Omega_\mathcal{T}$);

**Output**: $n_{p_{\text{End}}}$

### Numerical example

**Set-up** In the framework of section 2.3, we here consider the smallest possible zones, that is one parameter for each triangle of the reconstruction mesh. Figure 5 shows which zones are selected with three threshold values $\mathcal{T} = 10\%$, $\mathcal{T} = 20\%$ and $\mathcal{T} = 30\%$.

**Results** We can see that a threshold of $\mathcal{T} = 10\%$ yields an accurate selection of the perturbation, and thus provides a satisfactory reconstruction with only $N_{Sel} = 323$ selected parameters. Thus, we end up with significantly less parameters than the 2672 we have initially considered.

**Comments** We can also see in Table 2 that the relative error can be lower than what was obtained through a full Gauss-Newton reconstruction over a set of various configurations. This is a consequence of the fact that all the parameters outside the perturbation are equal to the exact value, while they can be miscalculated in the full reconstruction. Identifying the unperturbed parameters can thus clearly enhance the reconstruction. As previously, the stopping criterion was reached after four iterations in all cases.

| | | $15 \times 15$ data | | $30 \times 30$ data | | $60 \times 60$ data | |
|---|---|---|---|---|---|---|---|
| $\mathcal{T}$ | $\varepsilon$ | $N_{Sel}$ | $e_{p_{\text{End}}}$ | $N_{Sel}$ | $e_{p_{\text{End}}}$ | $N_{Sel}$ | $e_{p_{\text{End}}}$ |
| | 5% | 874 | 4.0% | 739 | 3.3% | 633 | 2.8% |
| 10% | 2% | 354 | 2.4% | 323 | 2.3% | 360 | 2.3% |
| | 1% | 305 | 2.3% | 282 | 2.4% | 296 | 2.3% |
| | 5% | 321 | 2.7% | 282 | 2.6% | 268 | 2.8% |
| 20% | 2% | 196 | 3.5% | 181 | 3.7% | 203 | 3.3% |
| | 1% | 172 | 4.1% | 162 | 4.3% | 171 | 4.0% |
| | 5% | 204 | 3.3% | 181 | 3.7% | 178 | 3.9% |
| 30% | 2% | 134 | 5.4% | 125 | 5.7% | 136 | 5.3% |
| | 1% | 120 | 5.8% | 112 | 5.9% | 115 | 5.8% |

Table 2: Selective reconstruction

However, a threshold of $\mathcal{T} = 20\%$ seems too high, as the 181 selected zones do not completely cover the perturbation's support, resulting in a slightly flawed reconstruction. More precisely, the relative error obtained as a function of $\mathcal{T}$ with $30 \times 30$ data can be seen in Figure 6. Clearly, there is an optimal value for $\mathcal{T}$ around 10% when the noise ratio is kept low.

Besides, with more noise (5%), we see in Figure 6 that the optimal $\mathcal{T}$ is shifted towards 20%. Furthermore, we see that a good estimation of this threshold becomes even more important when the noise level grows. This brings up the problem of how to select a correct threshold, taking at least the measurements noise and the amount of data into account. Unfortunately, for the moment, we do not have a realistic indicator to tell if the selected threshold is acceptable.

## 3.2 Adaptive refinement

As stated in section 2.3, we use a reconstruction mesh that is different from the one used to generate the data. Hence, the supports of the basis functions used in the reconstruction will not follow the geometry of $n^\star$, especially with a low number $N$ of basis functions. Thus, we propose to iteratively refine the reconstruction mesh with help of the previously introduced defect localization, in order to provide a satisfying approximation of the unknown index with a small number of parameters. The refinement outline is presented in Algorithm 3.

The number of 16 mesh elements is taken so that, after the splitting, each zone has still more than four mesh elements, which is the lower limit for defects to be relevant, as specified in Remark 3.2.

### Numerical example

**Set-up** We illustrate our adaptive refinement in Figure 7 in the same conditions as in section 3.1.

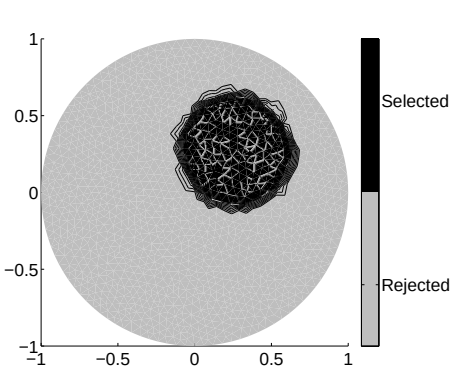


(a) Selected parameters ($N_{Sel} = 316$)

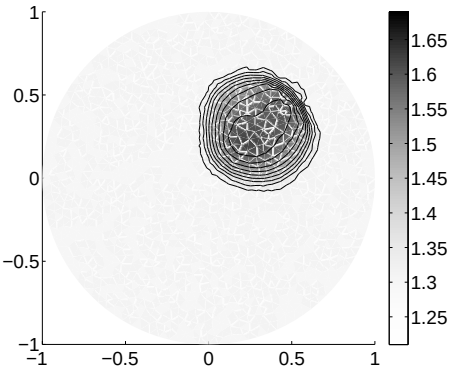

(b) Final index ($n_{p_{\mathrm{End}}}$)

Selection threshold $\mathcal{T} = 10\%$

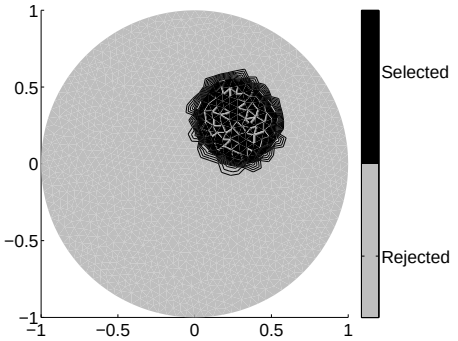


(c) Selected parameters ($N_{Sel} = 178$)

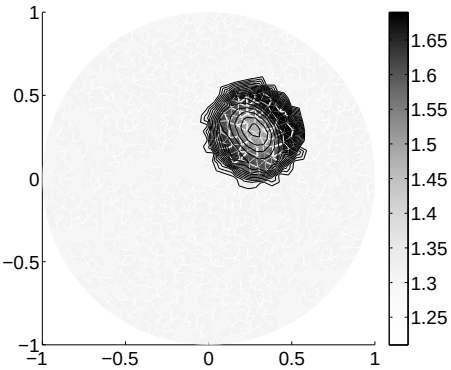

(d) Final index ($n_{p_{\mathrm{End}}}$)

Selection threshold $\mathcal{T} = 20\%$

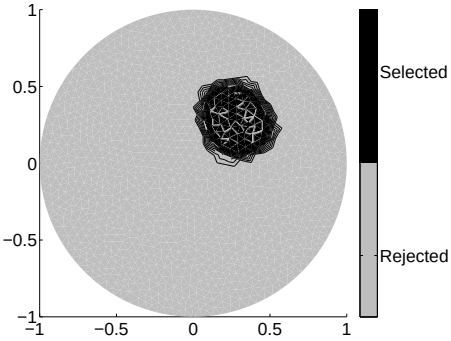


(e) Selected parameters ($N_{Sel} = 127$)

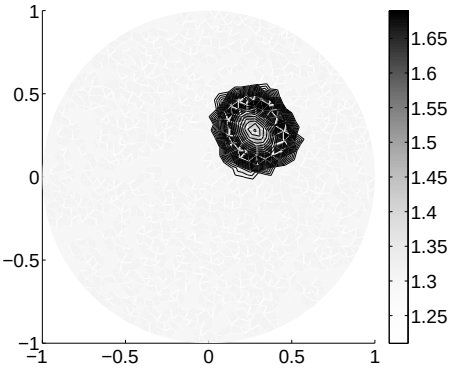

(f) Final index ($n_{p_{\mathrm{End}}}$)

Selection threshold $\mathcal{T} = 30\%$

Figure 5: Selective reconstruction with $30 \times 30$ data and $\varepsilon = 2\%$ noise

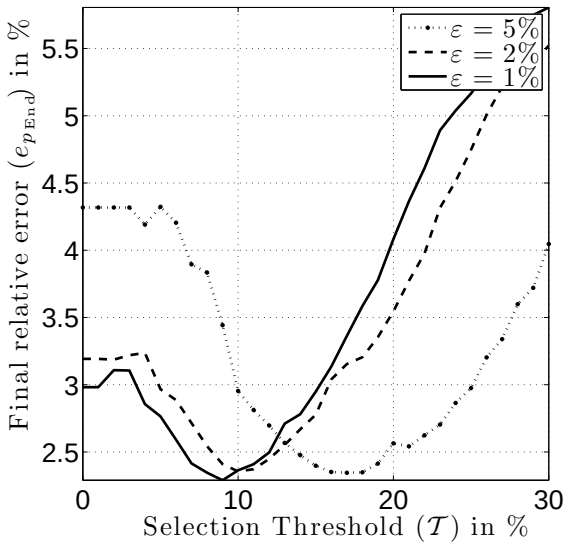


Figure 6: Influence of the threshold $\mathcal{T}$ with $30 \times 30$ data and different noise levels $\varepsilon$

**Algorithm 3:** Adaptive refinement

**Input**: $n_0 \in L^\infty(D)$

$p \leftarrow 0$;

**repeat**

  $\mathcal{S}_i \leftarrow \max_{Z_i} \mathcal{S}_{\{n_p, n^\star\}}(x)$;

  $I \leftarrow \{i$ such that $Z_i$ contains more than 16 mesh elements$\}$;

  $i_{\mathrm{Split}} \leftarrow i$ such that $\mathcal{S}_{i_{\mathrm{Split}}} = \max_{i \in I} \mathcal{S}_i$;

  Update the set of zones by splitting $Z_{i_{\mathrm{Split}}}$ into four sub-zones;

  Update the set of parameters accordingly by duplicating $\eta_{i_{\mathrm{Split}}}$ three times;

  $N \leftarrow N + 3$;

  $n_{p+p_{\mathrm{End}}} \leftarrow$ **Algorithm 1**($\mathbf{n_p}$);

  $p \leftarrow p + p_{\mathrm{End}}$;

**until** *$N > N_{\max}$ or each $Z_i$ contains less than 16 mesh elements*;

**Output**: $n_{p_{\mathrm{End}}}$

**Results** The steps 3 (defect localization) and 9 (reconstruction on the refined set) of Algorithm 3 are illustrated alternately in Figures 7a–7f, and it can be seen how the reconstruction focuses on the support of the contrasting perturbation. Figure 7g represents the values of $n_{59}$, which is obtained with $N = 76$ basis functions chosen during 25 successive adaptive refinements. Also, the relative error $e_p$, obtained in step 10 of the algorithm, is plotted in Figure 7h as a function of $p$.

**Comments** First, it can be noted that each refinement adds 3 parameters to be reconstructed and that each call to Algorithm 1 generates about four iterations (see Tables 1-2). So, the number of iterations is comparable to the number of parameters.

Then, comparing with the results obtained when using basis functions that are placed randomly, summarized in Table 1 or in Figure 3f, we can see lower reconstruction errors when using our guided adaptive refinement. In this example, our results are even comparable to the complete reconstruction (Algorithm 1) performed with 20 times more parameters. We thus meet our goal, which is a satisfactory reconstruction with a limited number of well-chosen basis functions.

Moreover, as we can see in Table 3, the sensitivities to noise or data amount in this example are similar to what we observe in section 3.1.

Finally, it cannot be overlooked that the number of total iterations $p_{\text{end}}$ is now quite high, since each loop in Algorithm 3 computes an iterative reconstruction. However each of those reconstructions is conducted on a very small number of parameters. So, the integral representation (7) for the differential is not cost effective in this case and a suitably tuned evaluation of $n_{p+1}$ in Algorithm 1 might thus be able to balance the higher number of iterations.

| | $15 \times 15$ data | | $30 \times 30$ data | | $60 \times 60$ data | |
|---|---|---|---|---|---|---|
| $\varepsilon$ | $N$ | $e_{p_{\text{End}}}$ | $N$ | $e_{p_{\text{End}}}$ | $N$ | $e_{p_{\text{End}}}$ |
| 5% | 76 | 4.9% | 76 | 6.0% | 76 | 5.0% |
| 2% | 76 | 4.0% | 76 | 4.8% | 76 | 3.3% |
| 1% | 76 | 3.8% | 76 | 4.4% | 76 | 3.6% |

Table 3: Adaptive refinement

# 4 Combining both strategies

The selective reconstruction is presented in section 3.1 as a preliminary step to the reconstruction. Furthermore, the adaptive refinement described in section 3.2 enhances the actual reconstruction step. So, adaptive refinement and selective reconstruction can be used one after the other. This extension of Algorithm 2 is described in Algorithm 4.

**Algorithm 4:** Selective reconstruction followed by adaptive refinement

**Input**: $n_0 \in L^\infty(D)$

1 $\mathcal{S}_i \leftarrow \max_{Z_i} \mathcal{S}_{\{n_0, n^\star\}}(x)$;

2 $\Omega_{\mathcal{T}} \leftarrow$ the set of zones on which $\mathcal{S}_i > \mathcal{T} \max(S_i)$;

3 $n_{p_{\text{End}}} \leftarrow$ **Algorithm 3**$(\mathbf{n_0}|_{\mathbf{\Omega}_{\mathcal{T}}})$ (all indices are extended by $n_0$ outside $\Omega_{\mathcal{T}}$);

**Output**: $n_{p_{\text{End}}}$

Note that the number of parameters selected in step 1 of this algorithm is not directly used in the adaptively refined reconstruction (step 3). Indeed, the iterative refinement described

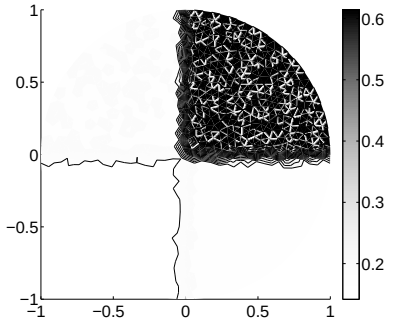


(a) Loop 1, step 3 (defect localization)

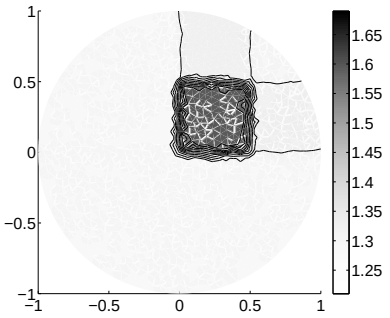


(b) Loop 1, step 9 (refined reconstruction)

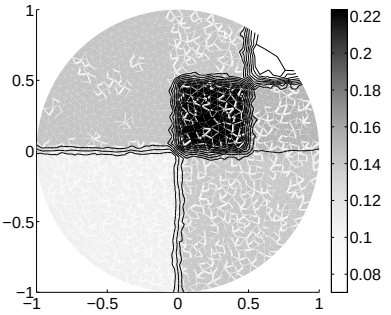


(c) Loop 2, step 3 (defect localization)

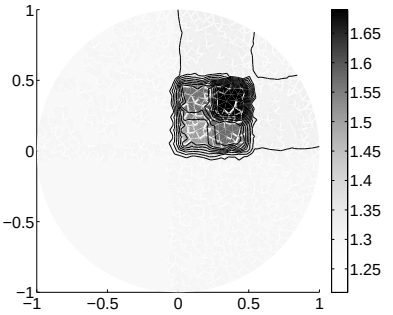


(d) Loop 2, step 9 (refined reconstruction)

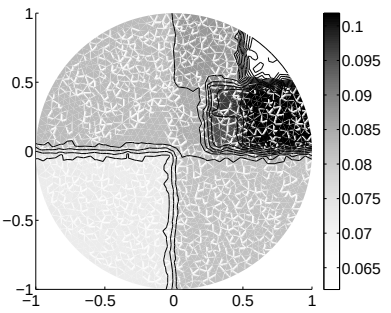


(e) Loop 3, step 3 (defect localization)

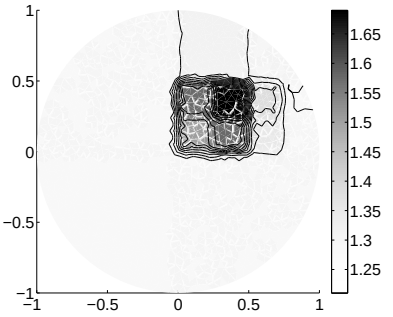


(f) Loop 3, step 9 (refined reconstruction)

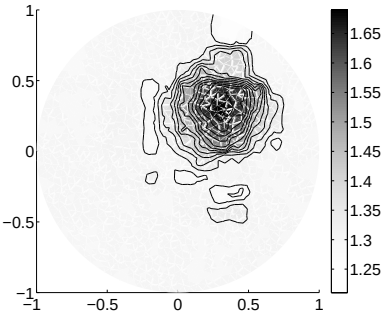


(g) Loop 25 (final), step 9

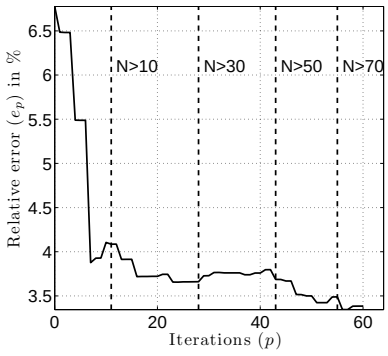


(h) Evolution of the relative error

Figure 7: Adaptive refinement (Algorithm 3) with $30 \times 30$ data and $\varepsilon = 2\%$ noise

in Algorithm 3 starts the reconstruction with only one zone. More precisely, the information retained from the selection step is the shape of the perturbation. Note that the accuracy of this selection is important: This is what allows the adaptive refinement to focus on the reconstruction of the perturbation's inner geometry, instead of focusing on the contrast between the perturbation and the background.

#### Numerical example 1

**Set-up** As in section 3, we illustrate Algorithm 4 with the selection thresholds $\mathcal{T} = 10\%$, $\mathcal{T} = 20\%$ and $\mathcal{T} = 30\%$. The respective selected mesh elements can be seen in Figures 5a–5e.

**Results** Figures 8a–8c show the reconstructions after 2, 4 and final adaptive refinement loops with a threshold $\mathcal{T} = 10\%$. As expected through the previous results, the reconstruction is very good. In fact, the exact values listed in Table 4 show that this reconstruction reaches an accuracy comparable to the one obtained through the initial selective reconstruction; the latter requiring 10 times more basis functions. As in section 3.2, and for the same reasons, the number of parameters for each adaptively refined reconstruction is comparable to the number of iterations.

Similarly to the examples presented in section 3.1, $\mathcal{T} \geqslant 20\%$ also provides a too small selection, leading to a flawed reconstruction. For example, it can be seen in Figures 8d–8i that the reconstruction tends to a crown shape. So, the constraint induced by this too small selection seems to create false local minima, altering he whole convergence process, as we can see in Figure 8j. The corresponding relative error values are detailed in Table 4.

**Comments** Since the selection is performed before the adaptive refinement, the choice of the threshold $\mathcal{T}$ still has a large influence in the final result, even in the case of over-selection. However, results in terms of accuracy remain close to the reference listed in Table 1 while involving only 0.6% to 2% of the total number of elements used in the full Gauss-Newton reconstruction.

| | | $15 \times 15$ data | | $30 \times 30$ data | | $60 \times 60$ data | |
|---|---|---|---|---|---|---|---|
| $\mathcal{T}$ | $\varepsilon$ | $N$ | $e_{p_{\text{End}}}$ | $N$ | $e_{p_{\text{End}}}$ | $N$ | $e_{p_{\text{End}}}$ |
| 10% | 5% | 60 | 3.9% | 57 | 3.1% | 61 | 3.1% |
| | 2% | 52 | 2.6% | 52 | 2.4% | 55 | 2.5% |
| | 1% | 49 | 2.6% | 52 | 2.5% | 52 | 2.5% |
| 20% | 5% | 52 | 3.3% | 52 | 2.8% | 46 | 3.0% |
| | 2% | 22 | 3.8% | 19 | 3.7% | 22 | 3.3% |
| | 1% | 19 | 4.0% | 19 | 3.9% | 16 | 4.1% |
| 30% | 5% | 16 | 4.1% | 19 | 3.6% | 16 | 4.2% |
| | 2% | 16 | 5.3% | 16 | 5.6% | 16 | 5.3% |
| | 1% | 15 | 5.5% | 16 | 5.6% | 16 | 5.6% |

Table 4: Selective reconstruction chained with iterative refinement

#### Numerical example 2

**Set-up** As a last example, we now consider a more elaborate and complex valued unknown index $n^\star$, shown in Figure 9. Besides, we also make this reconstruction more challenging by reducing the measurements aperture. Incoming directions are still taken in $[0, 2\pi]$, but there will be five less, and measurement directions are now taken in $[0, \frac{3}{2}\pi]$. In this situation, the

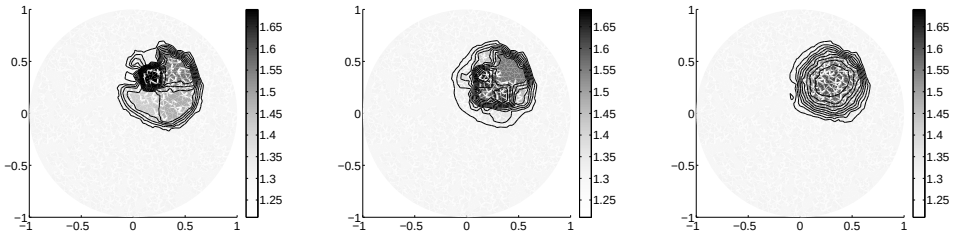

(a) Second refinement (b) Fourth refinement (c) Last ($17^{th}$) refinement

Selection threshold $\mathcal{T} = 10\%$

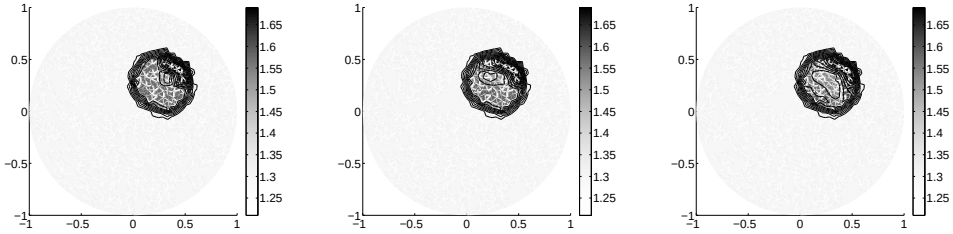

(d) Second refinement (e) Fourth refinement (f) Last ($8^{th}$) refinement

Selection threshold $\mathcal{T} = 20\%$

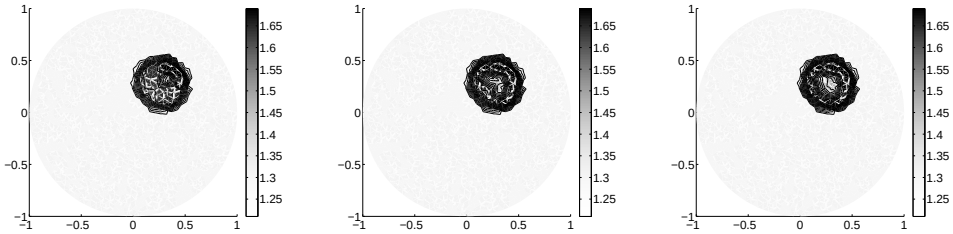

(g) Second refinement (h) Fourth refinement (i) Last ($5^{th}$) refinement

Selection threshold $\mathcal{T} = 30\%$

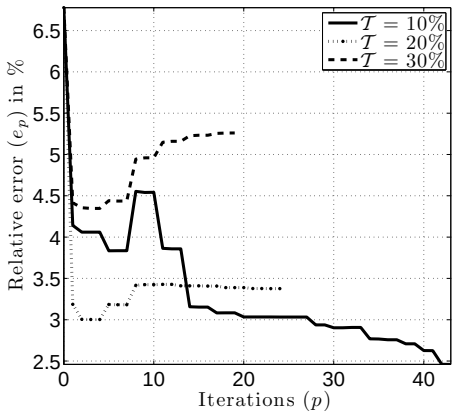


(j) Evolution of the relative error

Figure 8: Selective reconstruction followed by adaptive refinement, $30 \times 30$ data and $\varepsilon = 2\%$ noise

localization function presented in Theorem 3.1 cannot be defined. So, we consider the technical modification, recalled in Remark 3.2, that is conjectured to cover this case. Furthermore, we assume that $n^\star$ was known before the central perturbation. So, we consider the initial guess $n_0$ shown in Figure 10.

Finally, to remain in the previously defined context, we present the results of Algorithm 4 applied to this new geometry with the same selection thresholds $\mathcal{T} = 10\%$, $\mathcal{T} = 20\%$ and $\mathcal{T} = 30\%$.

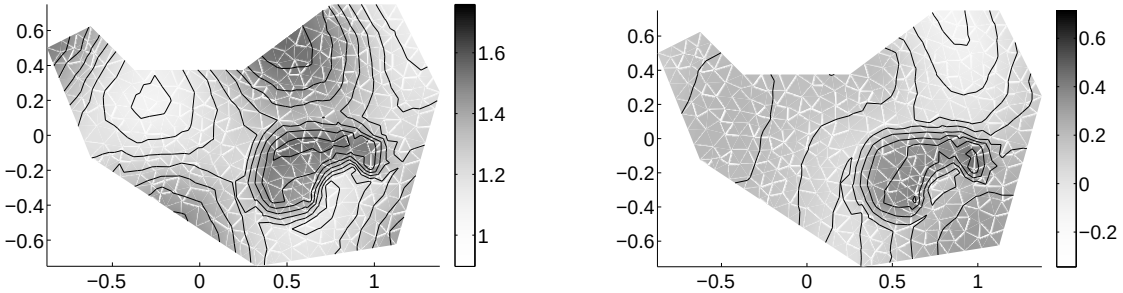


(a) Re $n^\star$ (b) Im $n^\star$

Figure 9: Exact index $n^\star$

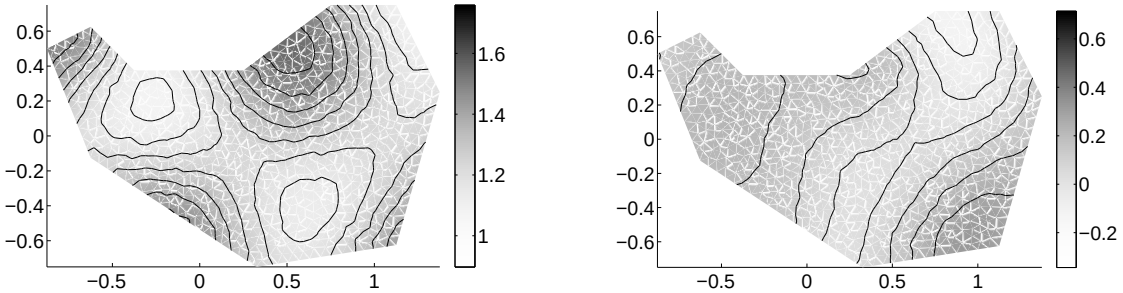


(a) Re $n_0$ (b) Im $n_0$

Figure 10: Initial guess $n_0$

**Results** The reference reconstructions obtained with the usual Gauss-Newton reconstruction (Algorithm 1) in the special case of $30 \times 25$ data and 2% noise are synthesized in Figure 11.

We then present in Figure 12 the selected zones and the resulting reconstruction corresponding to each selection threshold. In this case, $\mathcal{T} = 20\%$ now seems to be the best threshold value, and $\mathcal{T} = 30\%$ is still too high. Indeed, in the lines of the previous numerical example depicted in Figure 8, $\mathcal{T} = 30\%$ seems again to induce a false local minima, resulting in an altered convergence sequence. This is confirmed in Figure 12j, where we can also see that, even though $\mathcal{T} = 10\%$ allows to reach a satisfying precision, it requires much more refinements to do so than with $\mathcal{T} = 20\%$.

The results obtained in section 3 are thus reinforced by this example, exhibiting reconstructions comparable in precision to the full Gauss-Newton reconstruction, but with a much lower number of parameters.

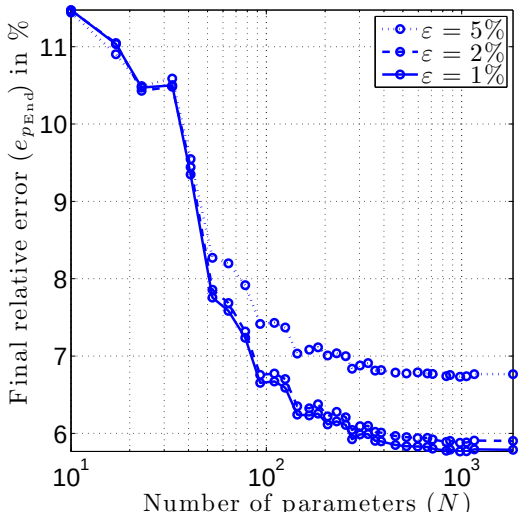


Figure 11: Relative error for the usual Gauss-Newton method, with $30 \times 25$ data and different noise levels $\varepsilon$

**Comments** Note that with this less trivial test case, the borders of the supports of the basis functions for the reconstruction do not correspond to the discontinuities of the exact index. This ensures that we avoid this particular case, which was mentioned in the concluding comments of Section 2.3.

# 5 Conclusion

We have used a defect localization method to propose two ways of reducing the number of parameters in the reconstruction of an unknown refraction index. The first method is set in the context of defects identification and uses their localization to reconstruct only the useful parameters of the whole index. The second method is an adaptive refinement, based on defect localization to iteratively reconstruct a better approximation with a limited number of parameters. We have obtained good numerical results with both methods.

The reconstruction could however be further enhanced by two automations: some automatic choice of the threshold for the defect localization function and some automatic selection of the regularization parameter. The second issue has been reviewed for example in [16, 17] and is claimed to be less critical when using a so-called Multiplicative Regularization described in [23]. However, for now, we have not been able to further enhance our results with these techniques. Finally, convergence of the coupled process, hybridizing the Gauss-Newton and Factorization methods, presented in this paper remains to be investigated.

# Acknowledgments

Support for some of the authors of this work was provided by the FRAE (Fondation de Recherche pour l'Aéronautique et l'Espace, `http://www.fnrae.org/`), research project IPPON.

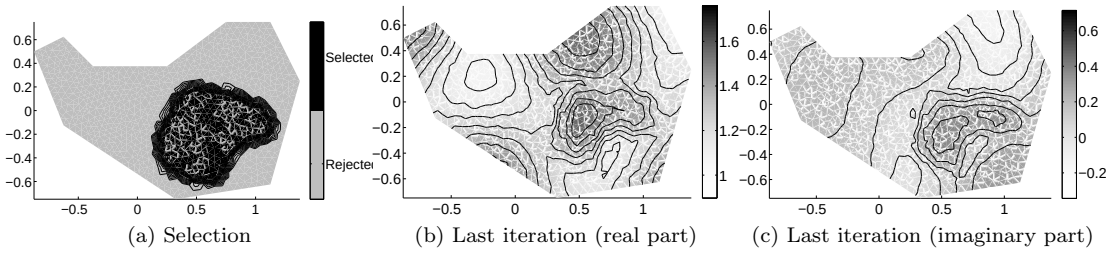


(a) Selection (b) Last iteration (real part) (c) Last iteration (imaginary part)

Selection threshold $\mathcal{T} = 10\%$

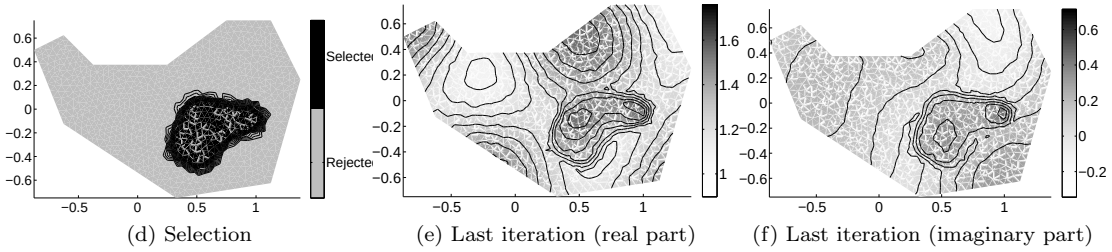


(d) Selection (e) Last iteration (real part) (f) Last iteration (imaginary part)

Selection threshold $\mathcal{T} = 20\%$

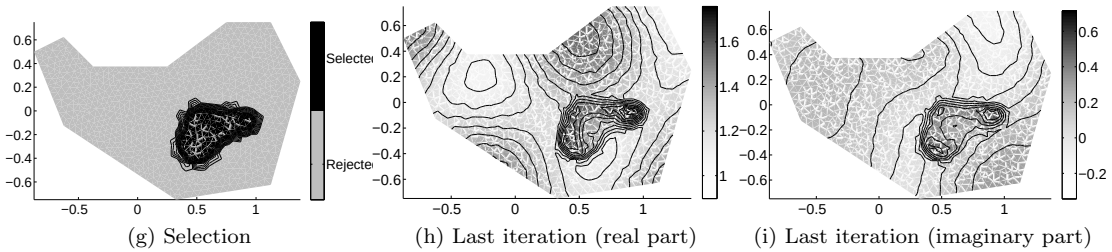


(g) Selection (h) Last iteration (real part) (i) Last iteration (imaginary part)

Selection threshold $\mathcal{T} = 30\%$

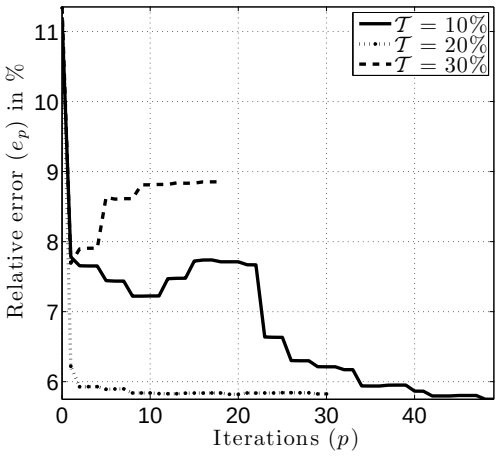


(j) Evolution of the relative error

Figure 12: Selective reconstruction chained with adaptive refinement for the more elaborate example with $30 \times 30$ data and $\varepsilon = 2\%$ noise

## References


[1] I. G. Scott and C. M. Scala. A review of non-destructive testing of composite materials. *NDT International*, 15(2):75–86, 1982.

[2] L. P. Song, C. Yu, and Q. H. Liu. Through-wall imaging (twi) by radar: 2-d tomographic results and analyses. *Geoscience and Remote Sensing, IEEE Transactions on*, 43(12):2793–2798, 2005.

[3] P. Mojabi and J. LoVetri. Microwave biomedical imaging using the multiplicative regularized gauss–newton inversion. *Antennas and Wireless Propagation Letters, IEEE*, 8:645–648, 2009.

[4] A. B. Bakushinsky and M. Y. Kokurin. *Iterative methods for approximate solution of inverse problems*, volume 577. Kluwer Academic Publishing, 2004.

[5] H. W. Engl, M. Hanke, and A. Neubauer. *Regularization of inverse problems*, volume 375. Springer Netherlands, 1996.

[6] Y. Grisel, V. Mouysset, P. A. Mazet, and J. P. Raymond. Determining the shape of defects in non-absorbing inhomogeneous media from far-field measurements. *Inverse Problems*, 28:055003, 2012.

[7] O. Bondarenko, A. Kirsch, and X. Liu. The factorization method for inverse acoustic scattering in a layered medium. *Inverse Problems*, 29(4):045010, 2013.

[8] R. Kress and P. Serranho. A hybrid method for sound-hard obstacle reconstruction. *J. Comput. Appl. Math.*, 204(2):418–427, 2007.

[9] M. Brignone, J. Coyle, and M. Piana. The use of the linear sampling method for obtaining super-resolution effects in Born approximation. *J. Comput. Appl. Math.*, 203(1):145–158, 2007.

[10] M. Brignone, G. Bozza, A. Randazzo, M. Piana, and M. Pastorino. A hybrid approach to 3d microwave imaging by using linear sampling and ACO. *Antennas and Propagation, IEEE Transactions on*, 56(10):3224–3232, 2008.

[11] G. Giorgi, M. Brignone, R. Aramini, and M. Piana. Application of the inhomogeneous Lippmann-Schwinger equation to inverse scattering problems. *SIAM J. Appl. Math.*, 73(1):212–231, 2013.

[12] D. Colton and R. Kress. *Inverse acoustic and electromagnetic scattering theory*, volume 93 of *Applied Mathematical Sciences*. Springer-Verlag, Berlin, second edition, 1998.

[13] A. Kirsch. *An introduction to the mathematical theory of inverse problems*, volume 120 of *Applied Mathematical Sciences*. Springer-Verlag, New York, 1996.

[14] L. Ségui. *Sur un problème inverse en diffraction d'ondes : identification de permittivités complexes d'un matériau à partir de données du champ proche*. PhD thesis, Université Toulouse III, 2000.

[15] P. Mojabi and J. LoVetri. Overview and classification of some regularization techniques for the Gauss-Newton inversion method applied to inverse scattering problems. *Antennas and Propagation, IEEE Transactions on*, 57(9):2658–2665, 2009.

[16] C. G. Farquharson and D. W. Oldenburg. A comparison of automatic techniques for estimating the regularization parameter in non-linear inverse problems. *Geophysical Journal International*, 156(3):411–425, 2004.

[17] F. S. V. Bazán and J. B. Francisco. An improved fixed-point algorithm for determining a Tikhonov regularization parameter. *Inverse Problems*, 25(4):045007, 16, 2009.

[18] A. B. Bakushinsky. The problem of the convergence of the iteratively regularized Gauss-Newton method. *Computational mathematics and mathematical physics*, 32(9):1353–1359, 1992.

[19] B. Blaschke, A. Neubauer, and O. Scherzer. On convergence rates for the iteratively regularized Gauss-Newton method. *IMA J. Numer. Anal.*, 17(3):421–436, 1997.

[20] A. I. Nachman, L. Päivärinta, and A. Teirilä. On imaging obstacles inside inhomogeneous media. *J. Funct. Anal.*, 252(2):490–516, 2007.

[21] B. Dah. *Sur la modélisation de milieux fictifs absorbants de type couches de Bérenger*. PhD thesis, Université Toulouse III, 2001.

[22] A. Kirsch and N. I. Grinberg. *The factorization method for inverse problems*, volume 36 of *Oxford Lecture Series in Mathematics and its Applications*. Oxford University Press, Oxford, 2008.

[23] P. M. van den Berg, A. L. van Broekhoven, and A. Abubakar. Extended contrast source inversion. *Inverse Problems*, 15(5):1325–1344, 1999.